

Development of a Chemical Toolset for Studying the Paralog-Specific Function of IRE1

Hannah C. Feldman,[†] Venkata Narayana Vidadala,[†] Zachary E. Potter,[†] Feroz R. Papa,^{§,||,⊥,#,▽} Bradley J. Backes,^{§,||} and Dustin J. Maly^{*,†,‡,⊞}

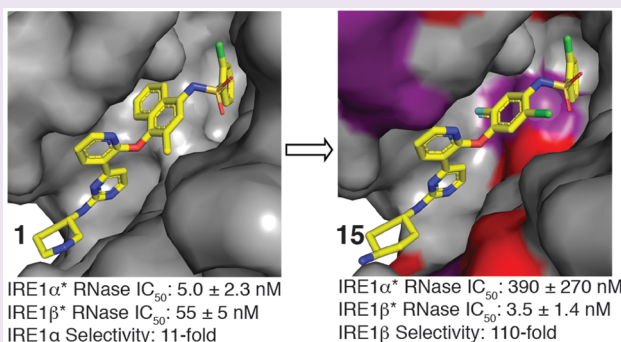
[†]Department of Chemistry, University of Washington, Seattle, Washington, United States

[‡]Department of Biochemistry, University of Washington, Seattle, Washington, United States

[§]Department of Medicine, ^{||}Lung Biology Center, [⊥]Department of Pathology, [#]Diabetes Center, [▽]California Institute for Quantitative Biosciences, University of California—San Francisco, San Francisco, California, United States

S Supporting Information

ABSTRACT: The dual kinase endoribonuclease IRE1 is a master regulator of cell fate decisions in cells experiencing endoplasmic reticulum (ER) stress. In mammalian cells, there are two paralogs of IRE1: IRE1 α and IRE1 β . While IRE1 α has been extensively studied, much less is understood about IRE1 β and its role in signaling. In addition, whether the regulation of IRE1 β 's enzymatic activities varies compared to IRE1 α is not known. Here, we show that the RNase domain of IRE1 β is enzymatically active and capable of cleaving an XBP1 RNA mini-substrate *in vitro*. Using ATP-competitive inhibitors, we find that, like IRE1 α , there is an allosteric relationship between the kinase and RNase domains of IRE1 β . This allowed us to develop a novel toolset of both paralog specific and dual-IRE1 α/β kinase inhibitors that attenuate RNase activity (KIRAs). Using sequence alignments of IRE1 α and IRE1 β , we propose a model for paralog-selective inhibition through interactions with nonconserved residues that differentiate the ATP-binding pockets of IRE1 α and IRE1 β .



Various perturbations within the cell can cause endoplasmic reticulum (ER) stress, resulting in unfaithful folding and the accumulation of proteins within the lumen of the ER.^{1,2} In mammalian cells, these perturbations result in the unfolded protein response (UPR), which consists of three transmembrane sensor proteins: IRE1, PERK, and ATF6.^{3–7} The initial aim of the UPR is to restore ER homeostasis, where all three UPR sensors initiate signals to upregulate genes that aid in ER stress adaptation.⁸ Additionally, PERK mediates a global translation block to help decrease the ER's protein folding burden.⁵ If these initial adaptive responses fail, the UPR switches to terminal outputs that result in apoptosis.⁹ IRE1 α is the most ancient and conserved component of the UPR and is thought to be one of the dominant factors in cell fate decision making in cells experiencing ER stress.^{4,10} IRE1 α contains a stress sensing N-terminal luminal domain that is connected to cytosolic protein kinase and RNase domains through a transmembrane linker.¹¹ Upon ER stress, IRE1 α becomes active through luminal domain dimerization and kinase *trans*-autophosphorylation. Phosphorylation of the kinase promotes IRE1 α dimerization on the cytosolic face of the ER, an event required for RNase domain activity.^{12,13} Under an adaptive UPR, the RNase domain of IRE1 α facilitates the cleavage of XBP1 mRNA, which results in the subsequent generation of a mature form of XBP1 that encodes

for an active transcription factor that upregulates targets that aid in ER adaptation.^{14–16} Conversely, prolonged ER stress leads to the cleavage of ER-localized mRNA by IRE1 α 's RNase in an event called regulated IRE1 dependent decay, or RIDD.^{17–19} RIDD increases ER stress and promotes apoptosis through the cleavage of mRNA encoding for adaptive ER proteins and antiapoptotic proteins, as well as cleaving miRNA functioning to suppress pro-apoptotic and pro-inflammatory proteins.²⁰

In mammalian cells, IRE1 α has a highly homologous paralog called IRE1 β . While IRE1 α is ubiquitously expressed, IRE1 β 's expression is mainly isolated to epithelial cells in the gastrointestinal tract and bronchia.²¹ IRE1 β 's domain architecture is the same as IRE1 α 's, but much less is known about its RNase activity or its functional role in the cell. While it has been shown that IRE1 β 's kinase retains phosphotransferase function, there have been conflicting reports about the ability of its RNase domain to cleave XBP1 and the efficiency of this cleavage event compared to IRE1 α .^{16,22} It has been suggested that under ER stress, rather than prioritizing XBP1

Received: June 17, 2019

Accepted: September 26, 2019

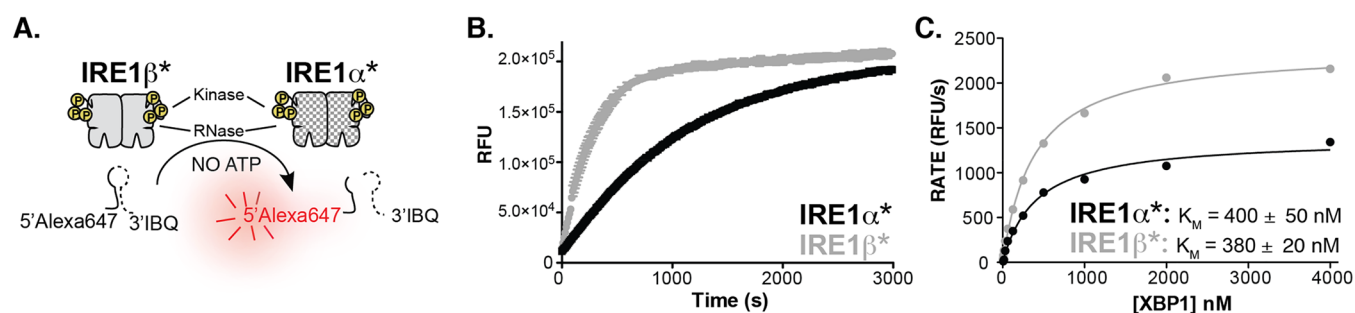


Figure 1. *In vitro* activity of IRE1 β 's RNase domain. (A) Schematic of the XBP1 cleavage assay with IRE1 α^* and IRE1 β^* . An increase in fluorescence is observed upon cleavage of a FRET-quenched XBP1 mini-substrate. (B) Real time fluorescence curves for 75 nM IRE1 α^* and 75 nM IRE1 β^* with 250 nM of the XBP1 mini-substrate. (C) Michaelis–Menten curves of IRE1 α^* and IRE1 β^* for the XBP1 mini-substrate. Data shown are mean \pm SEM, $n = 3$.

cleavage, IRE1 β 's RNase primarily cleaves ER-localized mRNA encoding secretory proteins.²³ Furthermore, there is evidence that IRE1 β might have a distinct set of mRNA substrates from IRE1 α .^{23–25} These differences in enzymatic activity have been highlighted *in vivo*, where IRE1 β but not IRE1 α has been shown to be functionally required for mucin production.²⁵ This relationship suggests that selective IRE1 β inhibition may be an attractive target in diseases characterized by the overproduction of mucin, like cystic fibrosis, chronic obstructive pulmonary disease, and asthma.²⁶ Additionally, mice that lack IRE1 β develop colitis at an advanced rate and have more pronounced hyperlipidemia, revealing that IRE1 β may play an essential role in lipid metabolism and inflammation responses in gut and bronchial tissues.^{21,27}

Here, we demonstrate that IRE1 β 's RNase domain is similarly efficient as IRE1 α in cleaving an XBP1 mini-substrate *in vitro*. Using different ATP-competitive inhibitors that have been shown to either activate or inhibit IRE1 α 's RNase activity, we investigated the allostery between IRE1 β 's kinase and RNase domains. We find that an ATP-competitive inhibitor that is a potent activator of IRE1 α 's RNase activity has a similar effect on IRE1 β . Furthermore, we demonstrate that, like IRE1 α , IRE1 β 's RNase activity can be allosterically inhibited with ATP-competitive ligands called kinase inhibitor RNase attenuators (KIRAs). This result motivated us to determine whether we could develop KIRAs that demonstrate paralog selectivity. By performing medicinal chemistry around the scaffold of a KIRA developed to target IRE1 α , we were able to identify both dual IRE1 α/β and paralog-selective KIRAs. Using a kinobead-based profiling method, we demonstrate that these inhibitors are selective for IRE1 on the kinome level. Together, we expect our IRE1-targeting toolset will provide valuable reagents for defining paralog-specific function in cells and disease models.

RESULTS AND DISCUSSION

Activity and Allosteric Regulation of IRE1 β 's RNase Domain. We first performed biochemical characterization of IRE1 β with a construct that contains just the cytosolic kinase and RNase domains, which we refer to as IRE1 β^* . Previous studies have demonstrated that a similar construct of IRE1 α , IRE1 α^* , possesses both kinase and RNase activity.^{28,29} For *in vitro* studies of IRE1, IRE1 α^* and IRE1 β^* were expressed in baculovirus-infected insect cells and purified in the activation loop phosphorylated form. Activation loop phosphorylation of IRE1 promotes the formation of an RNase active dimer, commonly referred to as the back-to-back dimer.¹³ In contrast,

dephosphorylated versions of IRE1 are monomeric and RNase inactive.^{28,29} To assess the RNase activities of IRE1 α^* and IRE1 β^* , we used a fluorescence-quenched XBP1 mini-substrate labeled with a 5'-AlexaFluor647 and a 3'-IowaBlack fluorescence quencher (Figure 1A). We tested the activity of IRE1 β^* 's RNase by monitoring the real-time cleavage of a XBP1 mini-substrate *in vitro*. Despite previous reports that IRE1 β 's RNase is less capable or incapable of cleaving XBP1,²² a comparison of equal concentrations of IRE1 α^* and IRE1 β^* reveal that both are able to efficiently cleave the XBP1 mini-substrate (Figure 1B). Further inspection of the XBP1 mini-substrate product revealed that the RNase domains of IRE1 α^* and IRE1 β^* generate fragments of similar size, supporting the notion that these paralogs cleave XBP1 at the same site (Supporting Information Figure 1). Next, we measured the rate of IRE1 α^* and IRE1 β^* cleavage for varying concentrations of the XBP1 mini-substrate to determine their Michaelis constant (K_M) values for this RNA substrate. The K_M values for the XBP1 mini-substrate between the two paralogs were nearly identical (Figure 1C). This result reveals that IRE1 β^* can form back-to-back dimers, which are necessary for RNase activity. Additionally, when dimerized, the RNase domains of IRE1 α^* and IRE1 β^* are similarly able to bind and cleave XBP1.

Previously, it has been established that the kinase and RNase domains of IRE1 α are allosterically coupled.^{28–30} The basis of this allostery relies on the conformation of a structural element in the ATP-binding site called helix- α C. When IRE1 α is unphosphorylated and inactive, helix- α C adopts a conformation that is incompatible with the back-to-back dimer required for RNase activity. Phosphorylation of IRE1 α 's activation loop stabilizes the active conformation of helix- α C, which promotes back-to-back dimerization and RNase activity.²⁹ It has been shown that ATP-competitive inhibitors can have divergent effects on IRE1 α 's RNase activity by preventing or promoting formation of the back-to-back dimer through modulation of helix- α C's conformation.^{13,28} For example, AT9283 potently activates IRE1 α 's RNase activity by promoting IRE1 α dimerization, presumably through stabilization of the active conformation of helix- α C.²⁹ In contrast, inhibitor 1 (KIRA8) inactivates IRE1 α 's RNase domain by stabilizing an inactive helix- α C conformation and preventing IRE1 α dimerization.³¹ We refer to ATP-competitive inhibitors that dually inhibit kinase and RNase activity, like 1, as kinase inhibitor RNase attenuators (KIRAs). To examine the allostery between the kinase and RNase domain of IRE1 β , we tested the effects of AT9283 and 1 on IRE1 β 's RNase activity. To allow us to

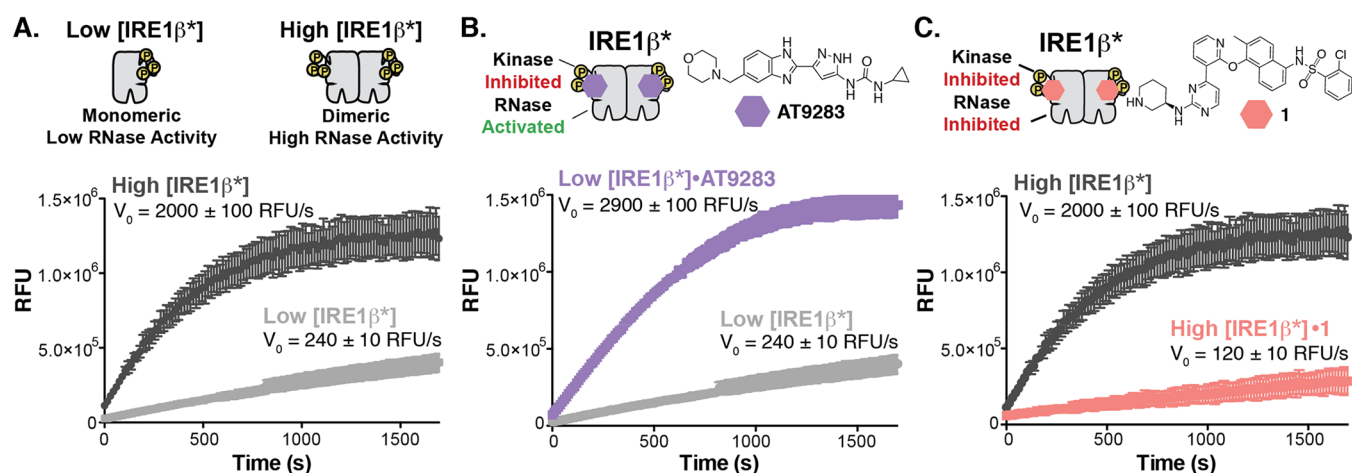


Figure 2. Divergent modulation of IRE1β's RNase domain with ATP-competitive inhibitors. (A) Concentration regimes for testing the allosteric modulation of IRE1β's RNase domain. (Top) Schematic of the oligomeric states of Low [IRE1β*] and High [IRE1β*]. (Bottom) Real time fluorescence curves and initial rates for Low [IRE1β*] and High [IRE1β*]. Data shown are mean \pm SEM, $n = 3$. (B) Activation of IRE1β's RNase activity. (Top) Structure of the ATP-competitive RNase activator AT9283. (Bottom) Real time fluorescence curves and rates of XBP1 mini-substrate cleavage for Low [IRE1β*] treated with DMSO (light gray) or AT9283 (purple) in the *in vitro* RNase assay. Data shown are mean \pm SEM, $n = 3$. (C) Inhibition of IRE1β's RNase activity. (Top) Structure of KIRA 1. (Bottom) Real time fluorescence curves and rates of XBP1 mini-substrate cleavage for High [IRE1β*] treated with DMSO (dark gray) or 1 (coral) in the *in vitro* RNase assay. Data shown are mean \pm SEM, $n = 3$.

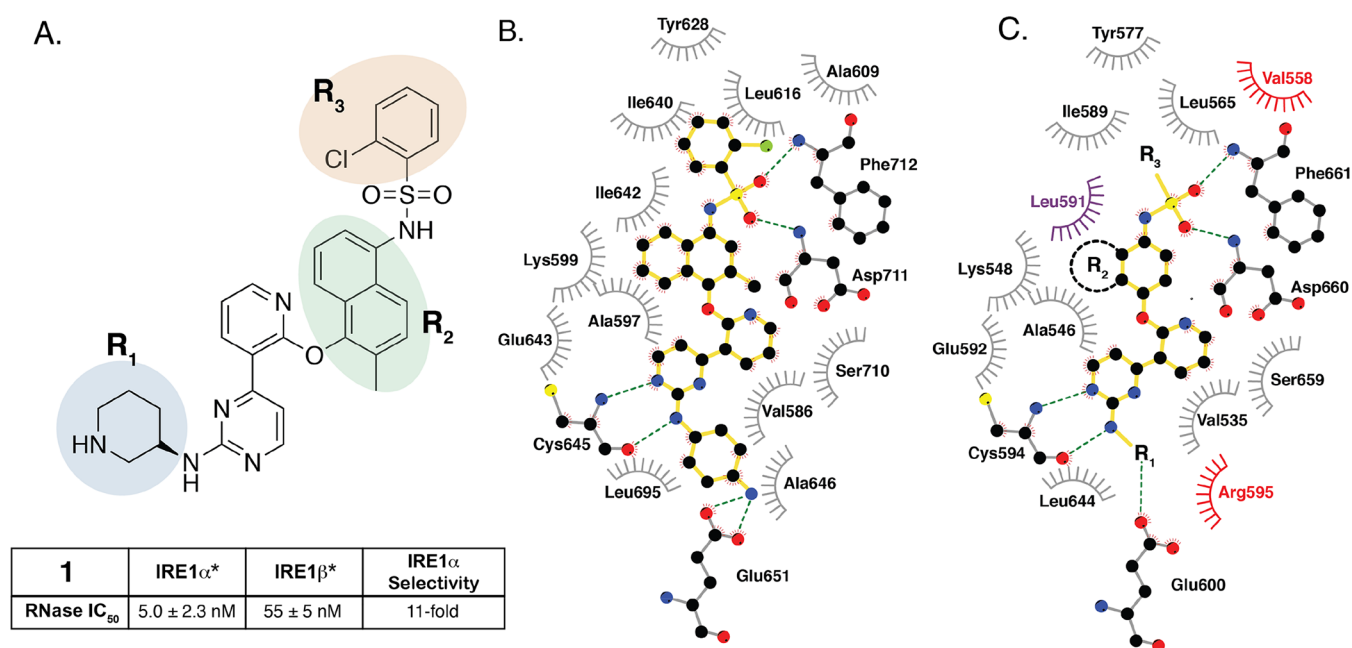
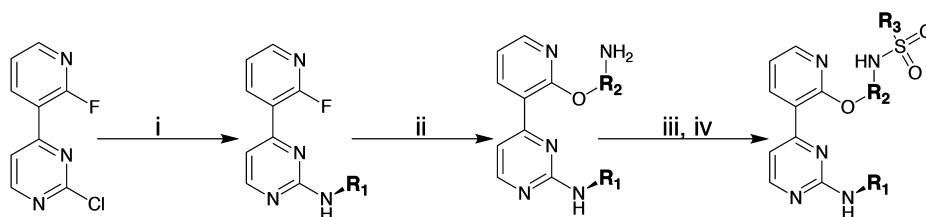


Figure 3. SAR of ATP-competitive KIRAs. (A) Chemical structure of KIRA 1 (top). Structural elements of 1 that are varied in our study are colored. RNase IC₅₀ values for 1 against both IRE1α* and IRE1β* and the fold selectivity for IRE1α (bottom). Inhibitor data are shown as the mean \pm SEM, $n = 3$. (B) LigPlot map detailing the binding interactions (yellow sticks) between inhibitor 2, a close analog of 1, and the ATP-binding site of IRE1α (PDB: 4U6R). Residues involved in hydrogen-bond interactions are shown as sticks. Residues involved in hydrophobic interactions are shown as gray eyelashes. (C) LigPlot map detailing the hypothesized binding pocket of IRE1β and its interactions with pyridine–pyrimidine-based ligands. Residues that are conserved between IRE1β and IRE1α are shown in gray. Conservative mutations are shown in purple, and nonconservative mutations are shown in red.

measure both activation and inhibition of RNase activity, we tested these inhibitors under two different IRE1β* concentration regimes. We used a concentration of IRE1β* (Low [IRE1β*]) that is mainly monomeric and has low RNase activity to measure activation of IRE1β's RNase activity by AT9283 (Figure 2A). A higher concentration of IRE1β* (High [IRE1β*]), which contains a substantial amount of the RNase active dimer, was used to test the inhibitory properties of KIRA

1. We found that Low [IRE1β*] treated with AT9283 demonstrated a 12-fold higher rate of XBP1 mini-substrate cleavage than the apo form (Figure 2B). In contrast, treatment of High [IRE1β*] with 1 led to an almost complete loss of its ability to cleave the XBP1 mini-substrate (Figure 2C). The ability of these two classes of ATP-competitive inhibitors to divergently modulate IRE1β's RNase activity suggests that

Scheme 1. Introduction of R₁–R₃ Groups into the Conserved Pyrimidine–Pyridine Scaffold of 1^a

^aReagents and conditions: (i) R₁-amine, TEA, DMSO, 80 °C, 18 h; (ii) 4-aminophenols, 5-aminonaphthols, or 4-aminonaphthols, K₂CO₃, DMF, 155 °C, μ W, 2 h; (iii) sulfonyl chloride, pyridine, DCM, RT, 18 h; (iv) TFA/DCM (1:1), RT, 2 h.

the allosteric communication between its kinase and RNase domains is similar to that of IRE1 α .

Paralog-Selective KIRAs. Having demonstrated that the RNase activity of IRE1 β can be modulated through its ATP-binding site, we next determined whether it would be possible to develop KIRAs with enhanced paralog selectivity. To do this, we performed a structure–activity-relationship (SAR) study around the pyrimidine–pyridine scaffold of KIRA 1 and a close analog (KIRA 2; Figure 3A,B). Although KIRAs 1 and 2 were optimized for IRE1 α , they were selected as starting points for derivatization because of the demonstrated marked selectivity of KIRA 1 on the kinome level.^{31,35} To visualize potential differences in KIRA-binding residues between IRE1 α and IRE1 β , we used a cocrystal structure of KIRA 2 bound to IRE1 α to generate a model of potential inhibitor contact residues with IRE1 β (Figure 3B,C). The basic *trans*-1,4-cyclohexanediamine moiety of 2 makes several hydrophobic contacts with residues lining the ATP-binding site of IRE1 α and forms a salt bridge with Glu651 located in IRE1 α 's helix α H. While IRE1 β contains a Glu at the same position (Glu600), an alanine residue (Ala646) in IRE1 α that makes hydrophobic contacts with the piperidine ring is substituted with an Arg (Arg595) in IRE1 β (Figure 3B,C). Therefore, we introduced various R₁ alicyclic groups that contain a basic amine in our SAR to potentially exploit these differences (Figure 3A). The naphthyl group of 2 bridges the core pyrimidine–pyridine scaffold and the sulfonamide group. While most of the residues in the ATP-binding site of IRE1 α that form contacts with the bridging naphthyl group of 2 are conserved in IRE1 β , the identity of the gatekeeper residue—Ile in IRE1 α (Ile642) and Leu in IRE1 β (Leu591)—is a clear difference between the two paralogs in this region of the binding pocket. We thus varied the naphthyl group of 2 with various naphthyl and substituted phenyl R₂ groups to see if inhibitors could differentiate between IRE1 α and IRE1 β in this region of the kinase active site. The arylsulfonamide of 2 occupies a pocket created by movement of helix- α C to an inactive conformation. A notable difference in this pocket between IRE1 α and IRE1 β includes a change from an Ala (Ala609) in the helix- α C of IRE1 α to a Val residue in IRE1 β (Val558). Therefore, we also generated analogs that contain various sulfonamides at the R₃ position to see if the pocket formed by the movement of helix- α C could be used to gain selectivity between IRE1 β and IRE1 α .

To facilitate the rapid generation of inhibitors, we introduced diverse R₁–R₃ groups into the conserved pyrimidine–pyridine scaffold of 1 (Scheme 1). A four-step synthetic route was used to diversify the commercially available 2-chloro-4-(2-fluoro-3-pyridinyl)pyrimidine scaffold. R₁ groups were introduced through the nucleophilic aromatic substitu-

tion (S_NAr) of 2-chloro-4-(2-fluoro-3-pyridinyl)pyrimidine with mono boc-protected diaminocycloalkanes. A subsequent S_NAr with commercially available 4-amino-phenols or aminonaphthols was used to generate R₂ group diversity. Diverse R₃ groups were introduced by sulfonylation with various sulfonyl chlorides. Following sulfonylation, final inhibitors were generated by boc-deprotection with TFA (Scheme 1).

We screened KIRAs for the ability to inhibit the RNase activities of IRE1 α * and IRE1 β * with our fluorescence-quenched XBP1 mini-substrate assay (Figure 1A). We first generated and tested an analog of 2 (inhibitor 3) that contains identical *trans*-1,4-cyclohexanediamine R₁ and 2-chlorophenyl R₃ groups but a slightly different 1,4-substituted 4-amino-1-naphthol R₂ group (Table 1). Inhibitor 3 is almost equipotent against IRE1 α * and IRE1 β *. Replacement of the *trans*-1,4-

Table 1. SAR of KIRAs Containing Naphthyl R₂ Groups^a

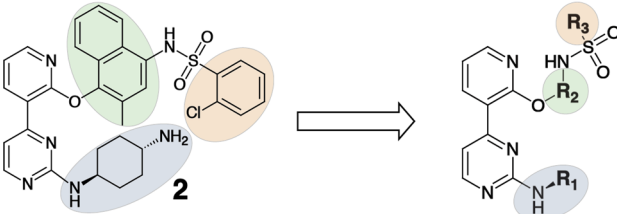
compd	R ₁	R ₂	R ₃	IRE1 β RNase IC ₅₀ (nM)	IRE1 α RNase IC ₅₀ (nM)	IRE1 β /RNase Selectivity (Fold)
1				55 ± 5	5.0 ± 2.3	0.09
3				15 ± 2	22 ± 9	1.4
4				100 ± 10	430 ± 230	4.2
5				490 ± 20	9.4 ± 1.0	0.02
6				>20000	10 ± 1	<0.0005
7				14000 ± 4000	42 ± 5	0.003

^aRNase IC₅₀ data are shown as mean ± SEM, *n* = 3. RNase selectivity was determined by dividing the IRE1 α * RNase IC₅₀ by the IRE1 β * RNase IC₅₀ value for each inhibitor (individual IC₅₀ curves provided in Supporting Information Figure 2).

cyclohexanediamine R_1 group with a 6-amino-2-aza-spiro[3.3]heptane moiety (inhibitor 4), while maintaining the same R_1 and R_3 groups as inhibitor 3, led to decreased inhibition of both IRE1 β 's and IRE1 α 's RNase domains, albeit disproportionately, resulting in 4.2-fold selectivity for IRE1 β *. Next, we explored whether R_3 sulfonamide groups affect paralog selectivity. Varying the R_3 group of 3 from a 2-chlorophenyl to a 2-chlorobenzyl group (inhibitor 5) led to a ~30-fold reduction in potency against IRE1 β 's RNase activity with minimal influence on IRE1 α * potency. We speculated that the Ala to Val substitution present in the helix- α C of IRE1 β would create a more restricted binding pocket that would favorably accommodate smaller R_3 groups. However, we found that inhibitor 6, which contains identical R_1 and R_2 substituents as inhibitor 3 but a smaller cyclobutyl R_3 group, is remarkably selective (>2000-fold) for IRE1 α *. Finally, we determined how changing the display of the R_3 sulfonamide from the R_2 naphthyl group would affect paralog potency and selectivity. We observed that inhibitor 7, which contains the same R_1 and R_3 groups as 6 but a 1,5-naphthyl substitution instead of a 1,4, was also highly selective (>300-fold) for IRE1 α *.

We found that a 4-amino-1-naphthol R_2 group provided inhibitors that are IRE1 α selective or equipotent for IRE1 α and IRE1 β while maintaining reasonably potent RNase inhibition (RNase IC₅₀ < 20 nM). To develop KIRAs that are potent and selective for IRE1 β , we next focused on optimizing the R_2 position for this paralog (Table 2). A notable difference between IRE1 α and IRE1 β is the identity of their gatekeeper residues. IRE1 α has an isoleucine residue (Ile642), while IRE1 β has a leucine (Leu591) at the gatekeeper position. This led us to reason that it may be possible to selectively target IRE1 β over IRE1 α by using smaller R_2 substituents, specifically substituted 4-aminophenol groups. First, we generated inhibitor 8, which contains a *trans*-1,4-cyclohexanediamine R_1 group, a 2-chlorophenyl R_3 group, and a 4-amino-3-fluorophenol at the R_2 position. Inhibitor 8, which contains the same R_1 and R_3 groups as IRE1 α /IRE1 β equipotent inhibitor 3, demonstrated single-digit nanomolar potency against IRE1 β * and is 5-fold selective for this paralog over IRE1 α *. Thus, replacing the 4-amino-1-naphthol R_2 group of 3 with a 4-amino-3-fluorophenol increased IRE1 β * selectivity. Replacing the *trans*-1,4-cyclohexanediamine R_1 group of 8 with an (S)-3-aminopiperidine (inhibitor 9) resulted in less potent inhibition of IRE1 α * and IRE1 β *. An analog of 9 that contains a 2-chlorobenzylsulfonamide (10) was found to be almost 10-fold selective for IRE1 α * over IRE1 β *.

For all inhibitors tested, we found that varying away from a 2-chlorophenylsulfonamide R_3 group was detrimental to IRE1 β * potency. Thus, for the remainder of inhibitors generated in this SAR study, a 2-chlorophenylsulfonamide group was maintained at the R_3 position. Because the introduction of a 4-amino-3-fluorophenol R_2 group modestly improved selectivity for IRE1 β * (compare inhibitor 3 to inhibitor 8), we next determined whether increasing the size of the halogen at this position could enhance the ability to discriminate between the two paralogs. Unfortunately, inhibitors containing a 4-amino-3-chlorophenol (11 and 12) were markedly less potent against IRE1 β *. We next determined the effect of changing the position of the halogen from the 3-position to the 2-position on the 4-aminophenol R_2 group by generating inhibitors 13 and 14, which contain 4-

Table 2. KIRAs Containing 4-aminophenol R_2 Groups^a


compd	R_1	R_2	R_3	IRE1 β RNase IC ₅₀ (nM)	IRE1 α RNase IC ₅₀ (nM)	IRE1 β RNase Selectivity (Fold)
8				4.4 ± 0.7	22 ± 9	5.0
9				120 ± 40	120 ± 10	1.0
10				50 ± 2	6.0 ± 1.7	0.12
11				99 ± 56	57 ± 11	0.57
12				150 ± 30	130 ± 70	0.87
13				3.9 ± 1.1	240 ± 50	60
14				13 ± 2	110 ± 10	8.1
15				3.5 ± 1.4	390 ± 270	110
16				430 ± 70	2000 ± 100	4.5
17				74 ± 14	270 ± 70	3.6
18				17 ± 2	83 ± 8	5.8

^aRNase IC₅₀ data are shown as mean ± SEM, $n = 3$. RNase selectivity was determined by dividing the IRE1 α RNase IC₅₀ by the IRE1 β RNase IC₅₀ value for each inhibitor (individual IC₅₀ curves provided in Supporting Information Figure 2).

amino-2-fluorophenols. Both inhibitors demonstrated promising selectivity for IRE1 β *, with inhibitor 13, which contains a *trans*-1,4-cyclohexanediamine R_1 group, exhibiting single-digit nanomolar potency against IRE1 β * and 60-fold selectivity over IRE1 α *. Finally, we looked at how adding an additional halogen to the 4-amino-2-fluorophenol R_2 group affected the potency and paralog selectivity of inhibitors. Inhibitor 15, which contains a 4-amino-5-chloro-2-fluorophenol R_2 group and a *trans*-1,4-cyclohexanediamine R_1 group, demonstrated potent inhibition of IRE1 β * and >100-fold selectivity over IRE1 α *. Replacing the *trans*-1,4-cyclohexanediamine R_1 group of 15 with an (S)-3-aminopiperidine (16) led to reduced potency against IRE1 β * and diminished selectivity. The addition of a fluorine to the 3- or 5-positions (inhibitor 17 and 18, respectively) of the 4-amino-2-fluorophenol R_2 group

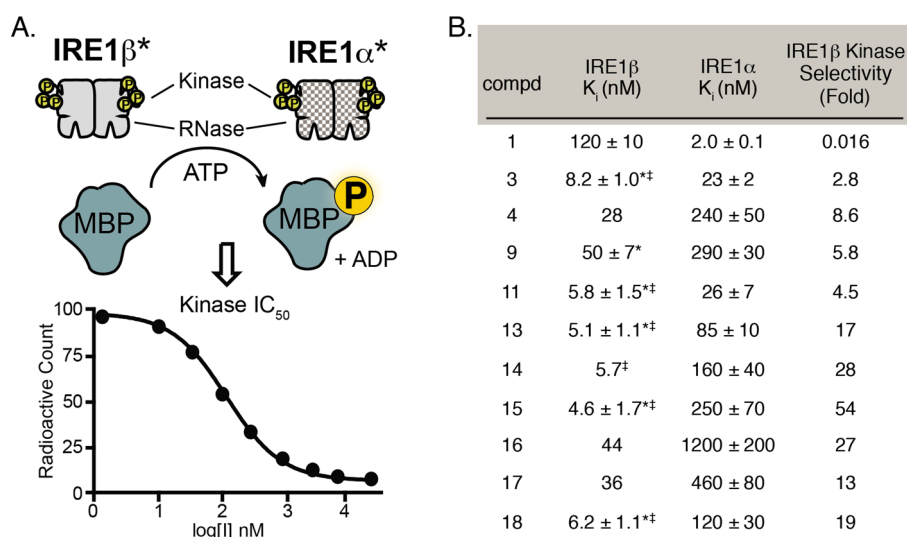


Figure 4. Kinase inhibition by exemplary KIRAs. (A) Schematic of the *in vitro* IRE1 kinase assay. Phosphotransferase activity of IRE1 was measured by monitoring the IRE1 α^* /IRE1 β^* -mediated phosphorylation of the exogenous substrate myelin basic protein (MBP) by ATP [γ - 32 P]. (B) K_i values for IRE1 α^* and IRE1 β^* kinase activity. All K_i values were calculated using the Cheng-Prusoff equation. For IRE1 α^* , the K_i values shown are mean \pm SEM, $n = 3$. For IRE1 β , the K_i values shown are the mean \pm SEM, $n = 3$ (denoted by an asterisk (*)) or the average values from two measurements (individual inhibitory values provided in Supporting Information Table 1). Inhibitors with K_i values lower than the concentration of IRE1 α^* or IRE1 β^* used in the assay are denoted with a double dagger (\ddagger). Individual IC_{50} curves provided in Supporting Information Figure 2.

was found to be generally detrimental to IRE1 β^* inhibition. From this SAR, it is clear that employing 4-amino-2-halophenol R_2 groups and a *trans*-1,4-cyclohexanediamine R_1 substituent can impart high IRE1 β RNase selectivity.

KIRAs Inhibit the Kinase Activity of IRE1 α/β . KIRA 1 was previously confirmed to be an ATP-competitive inhibitor of IRE1 α , and we assumed that all of the analogs generated in this study inhibit IRE1 RNase activity through the ATP-binding site.³¹ To verify that our inhibitors also inhibit the kinase activities of IRE1 α^* and IRE1 β^* , we measured the propensity of a representative set of compounds to block IRE1-mediated phosphorylation of an exogenous substrate—myelin basic protein (MBP; Figure 4A). As expected, we found that all compounds tested also inhibited the kinase activity of IRE1 α^* and IRE1 β^* (Figure 4B). While we were not able to accurately determine kinase IC_{50} values for a number of our more potent inhibitors (3, 11, 13, 14, 15, and 18) against IRE1 β^* due to constraints of the assay, we found that kinase IC_{50} values were, in general, several-fold lower than RNase IC_{50} values for this paralog. This is in contrast to IRE1 α^* , where inhibitors generally exhibited similar IC_{50} values against kinase and RNase activity. The reason for this discrepancy between the two paralogs is unknown but may reflect differences in the energetic penalties required to disrupt the dimeric states of IRE1 α^* and IRE1 β^* , and, in turn, RNase inhibition. Thus, inhibitors typically demonstrate slightly greater selectivity for IRE1 β^* in the kinase assay than in the RNase assay. Collectively, these results show that trends in inhibitor selectivity are consistent in both kinase and RNase assays.

Kinome Selectivity of Paralog-Selective KIRAs. From our optimization efforts, we were able to generate inhibitors with three different profiles: IRE1 α -selective inhibitors, dual-IRE1 inhibitors that are equipotent against IRE1 α and IRE1 β , and IRE1 β -selective inhibitors. Inhibitors with these profiles would be excellent tools for examining the contributions of IRE1 α and/or IRE1 β activity in cells if they possess sufficient general kinase selectivity. Therefore, we used a lysate profiling

method to determine if representative inhibitors from these three classes are selective on the kinome level. Specifically, we measured the abilities of representative inhibitors to compete for binding of lysate kinases to an affinity matrix containing seven different nonselective ATP-competitive inhibitors (kinobeads).^{32–34} Kinobeads enrich kinases through their ATP-binding sites and allow inhibitors to be quantitatively profiled against a large percentage of the human kinome. Binding of an inhibitor prevents enrichment with the kinobead matrix, and kinome selectivity can be determined by comparing the relative enrichment of a kinase target between DMSO and inhibitor-treated lysates using quantitative mass spectrometry (Supporting Information Figure 3). In total, we profiled five inhibitors (1 (IRE1 α -selective), 4 and 9 (dual-IRE1), and 13 and 15 (IRE1 β -selective)) with an HCT116/HEK293 cell lysate mixture spiked with exogenous recombinant IRE1 β^* (or IRE1 α^* for profiling of 1). The addition of exogenous IRE1 was required because we were not able to reproducibly quantify the endogenous protein.

The kinome selectivity of 1 was previously assessed with *in vitro* activity assays against a large panel of recombinant kinases, where it was shown to be highly selective across the kinome.^{31,35} These results were verified in our kinobead assay, where IRE1 α was the only kinase identified as a target of 1 (Supporting Information Figure 4). Out of \sim 150 kinases quantified in the assay, IRE1 β was the primary target of 3, 9, 13, and 15, with only one off-target identified for each respective inhibitor (Figure 5). Inhibitor 3, which contains a naphthol R_2 group, prevented the enrichment of PKD2 in addition to IRE1 β . Compounds 9, 13, and 15, which all contain 4-amino-halophenol R_2 groups, share the same off target, CDK2. To determine whether the level of competition observed in our kinobead assay would lead to potent inhibition of CDK2 activity, we tested the ability of 9, 13, and 15 to inhibit the CDK2/cyclin A complex *in vitro*. Despite the ability of 9, 13, and 15 to moderately prevent CDK2 binding to the kinobead matrix in our lysate profiling experiments (Support-

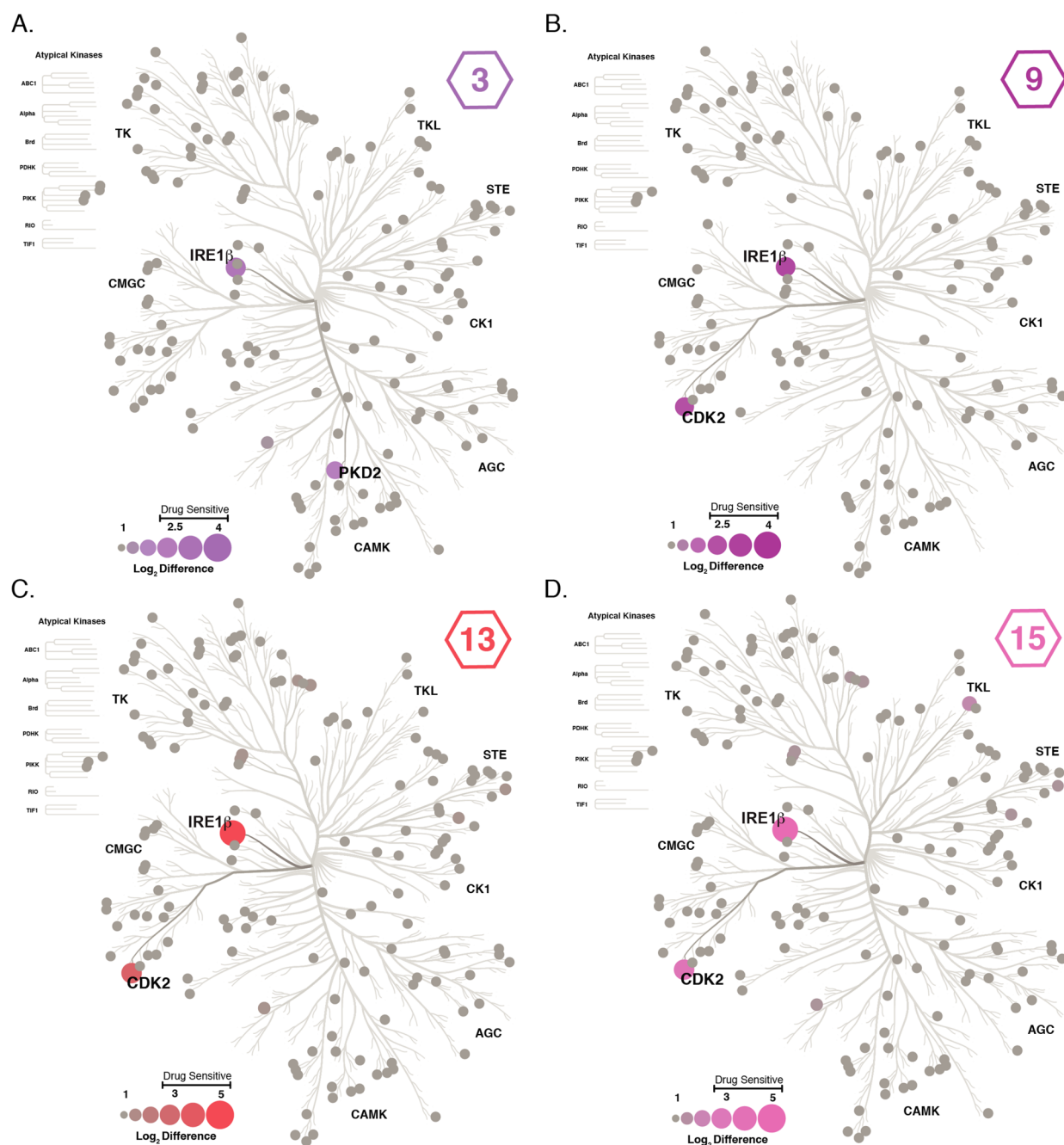


Figure 5. Kinome profiling of KIRAs 3, 9, 13, and 15. The kinome selectivities of 3, 9, 13, and 15 were determined with a previously described kinobead lysate profiling method. Kinases that were quantified in the experiment are shown as circular nodes, where node size and color have been scaled to the \log_2 difference (difference in LFQ intensity between DMSO treated and inhibitor treated lysates) between DMSO and treatment with 10 μ M of KIRA 3 (A), 9 (B), 13 (C), or 15 (D). Gray nodes represent kinases that were quantified, but no competition with an inhibitor was observed. Values shown are the mean of four replicates.

ing Information Figure 5A), all three KIRAs showed weak inhibition of CDK2/cyclin A kinase activity (IC_{50} values > 5 μ M; Supporting Information Figure 5B). For 9, 13, and 15, the discrepancy between the activity assay with CDK2/cyclin A and our kinobead profiling experiment could possibly be due to the high concentrations (10 μ M) of these inhibitors tested in the profiling experiment, which allows sufficient occupation of CDK2's ATP-binding site despite their weak affinities for this kinase. Another possibility is that these inhibitors can only interact with inactive CDK2, but not active CDK2-cyclin complexes. Previously, it has been shown that cyclin binding

causes a conformational change in CDK2's ATP-binding site that makes it inaccessible to certain types of ATP-competitive inhibitors.³⁶

Structural Model of Inhibitor Paralog Selectivity.

While extensive structural characterization has been performed with IRE1 α , equivalent information is not available for IRE1 β .^{29,31,37–42} To build a structural model of IRE1 β inhibition and selectivity, we used a sequence alignment of the kinase and RNase domains of IRE1 α and IRE1 β . The kinase domains of IRE1 α and IRE1 β share 81% sequence identity, while the RNase domains are 61% identical (Figure

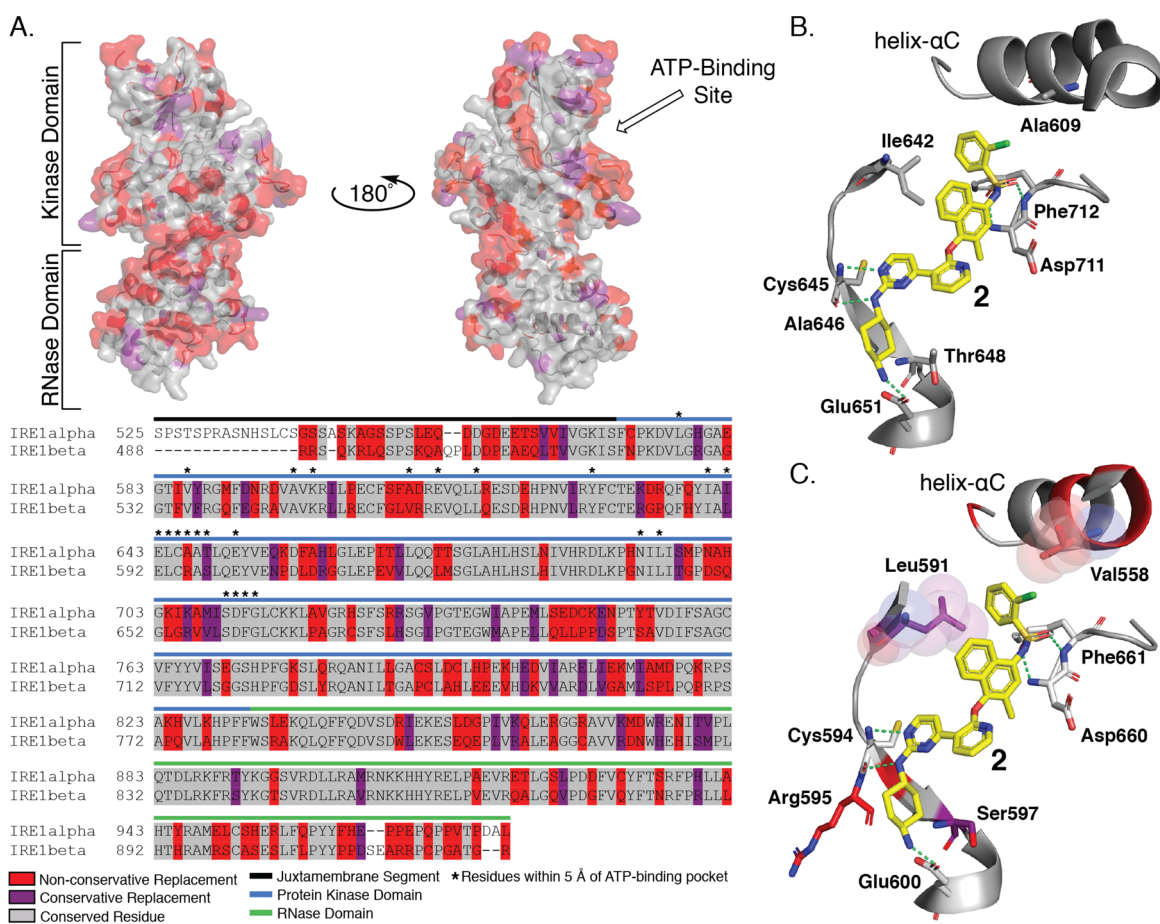


Figure 6. Sequence alignment and structural comparison of IRE1 α and IRE1 β ATP-binding sites. (A) Sequence alignment of IRE1 α and IRE1 β . (Top) Sequence comparison between IRE1 α and IRE1 β mapped onto the crystal structure of IRE1 α (PDB: 4U6R). Residues that are conserved are shown in gray, residues that have a conservative replacement are shown in purple, and residues with nonconservative replacements are shown in red. (Bottom) Sequence alignment of IRE1 α and IRE1 β shows 80% sequence identity of the kinase domain and 61% sequence identity of the RNase domain. (B) Interactions between 2, a close structural analog of KIRA 1, and the ATP-binding site of IRE1 α . Compound 2 is shown as yellow sticks, key interacting residues are shown as gray sticks, and interactions are denoted with green dashed lines. (C) Hypothesized binding mode of KIRA 2 by mapping of nonidentical residues of IRE1 β onto the structure of 4U6R. Conservative replacement nonidentical residues are shown as purple sticks; nonconservative nonidentical residues are shown as red sticks. Residue numbering is for IRE1 β .

6A).²⁴ Due to the high degree of sequence identity between the kinase domains of the two paralogs, we predicted that KIRAs would have similar binding modes in their ATP-binding sites. From our sequence alignment, we mapped sequence differences between IRE1 α and IRE1 β onto a cocrystal structure of IRE1 α bound to the pyrimidine–pyridine KIRA 2 (PDB: 4U6R).³¹ KIRA 2 is nearly identical to potent dual-IRE1 inhibitor 3, differing only by the presence of a methyl group at the 2-position of the R₂ naphthyl ring. Using the mutagenesis tool in PyMol, residue side chain differences between IRE1 α and IRE1 β were visualized for the cocrystal structure of IRE1 α bound to 2. We next looked at residues within 5 Å of inhibitor 2. Of the 23 residues identified, only four residues are not identical in IRE1 α and IRE1 β : Ala609 (Val558 in IRE1 β), Ile642 (Leu591 in IRE1 β), Ala646 (Arg595 in IRE1 β), and Thr648 (Ser597 in IRE1 β ; Figure 6B,C). Although the specific interactions that each paralog makes with inhibitors cannot be known in the absence of high-resolution structural information, these sequence differences likely play a major role in paralog selective inhibition. The IRE1 α residues Ala646 (Arg595 in IRE1 β) and Thr648 (Ser597 in IRE1 β) are directed toward the alicyclic portion of 2's *trans*-1,4-cyclohexanediamine R₁ group, which forms a salt

bridge with Glu651 in IRE1 α and most likely Glu600 in IRE1 β . While we were unsuccessful in identifying R₁ groups that were optimal for IRE1 β 's Arg595 and Ser597 residues, our SAR data show that IRE1 α is more permissive of variability at this position. The stabilization of an inactive helix- α C "out" conformation by KIRAs leads to IRE1 monomerization and RNase inhibition. The 2-chlorophenyl aryl sulfonamide R₃ group of 2 occupies the pocket created by movement of helix- α C. In this inactive conformation, Ala609 in IRE1 α (Val559 in IRE1 β) from helix- α C is projected toward inhibitor R₃ groups. Our SAR data demonstrate that the smaller Ala residue of IRE1 α allows it to favorably accommodate a greater diversity of R₃ substituents than IRE1 β . Finally, the side chain of IRE1 α 's gatekeeper residue, Ile642, points directly toward the methyl naphthyl R₂ group of 2 (Figure 6B). Interestingly, selectivity for IRE1 β , which possesses a Leu gatekeeper, over IRE1 α was achieved most effectively by introducing 4-amino-2-fluorophenol R₂ groups. Thus, we hypothesize that 4-amino-2-fluorophenol R₂ groups are able to form more favorable interactions with the Leu residue of IRE1 β than with the Ile residue of IRE1 α and that paralog selectivity can be achieved by optimizing gatekeeper/R₂ group interactions.

Conclusion. Pharmacological modulation of IRE1 α 's RNase domain using ATP-competitive inhibitors has proven to be a useful method for examining the allosteric relationship between the kinase and RNase domains of IRE1 α , and for better understanding the functional outputs of IRE1 α 's RNase domain. While IRE1 α 's close paralog IRE1 β shares the same domain architecture, much less is known about the enzymatic activities of IRE1 β and its function within the cell. Understanding IRE1 β 's role in the cell has been particularly difficult to determine because, while IRE1 β expression is limited to epithelial cells of the gut and bronchia, all cells that express IRE1 β also express IRE1 α . Pharmacological tools that are able to discriminate between IRE1 α and IRE1 β will be useful reagents for defining paralog-specific function in cells.

There have been conflicting reports on how efficiently the RNase domain of IRE1 β is able to cleave XBP1 mRNA.^{16,22} Here, we show that a cytosolic construct of IRE1 β (IRE1 β^*) has RNase activity comparable to IRE1 α^* for an XBP1 mini-substrate. Therefore, IRE1 β , like IRE1 α , appears to form dimers that bind and cleave XBP1 mRNA *in vitro*. A reason for the observed discrepancies in IRE1 β 's ability to cleave XBP1 may stem from differences in the phosphorylation state of the activation loop, which promotes formation of the RNase-active dimer, in the recombinant constructs used. The recombinant IRE1 β^* construct used in our study contains a glutathione S-transferase (GST) tag at its N-terminus. GST has been demonstrated to form dimers,⁴³ which likely enhances IRE1 β^* activation loop autophosphorylation when being expressed in insect cells. The N-terminal GST tag may also directly promote formation of RNase-active back-to-back dimers in the absence of activation loop phosphorylation. Regardless of the source of these discrepancies, our data clearly show that IRE1 β can efficiently cleave an XBP1 mini-substrate when it is dimerized. The implications of our results for the ability of full-length IRE1 β to cleave XBP1 mRNA in cells is unclear. In cells, IRE1 β 's ability to undergo activation loop autophosphorylation appears to be hampered compared to its paralog IRE1 α .⁴⁴ Therefore, XBP1 mRNA may be a poor substrate for IRE1 β in cells because the kinase domain does not undergo activation loop phosphorylation under ER stress. Differences in the ability of IRE1 α and IRE1 β to undergo autophosphorylation may also help explain previously reported disparities in the mRNA substrate preference between these two paralogs in cells. Under ER stress, XBP1 mRNA may be cleaved by activation loop phosphorylated IRE1 α while IRE1 β functions to aid in later stages of the UPR by cleaving ER-localized mRNAs as a part of RIDD.^{23–25}

To examine the allosteric relationship between IRE1 β 's kinase and RNase domains, we report the first ATP-competitive pharmacological modulators of IRE1 β . We show that ATP-competitive inhibitors that activate IRE1 α 's RNase domain also activate IRE1 β 's RNase domain. Additionally, we find that ATP-competitive KIRAs are capable of inhibiting IRE1 β 's RNase activity like IRE1 α 's. The ability of ATP-competitive inhibitors to divergently modulate the RNase activity of IRE1 β suggests that it shares all or most of the allosteric features of IRE1 α .

By generating analogs of a KIRA that are moderately selective for IRE1 α , we were able to identify inhibitors with two new paralog selectivity profiles: KIRAs that are equipotent against IRE1 α and IRE1 β and KIRAs that are highly selective for IRE1 β . Lysate profiling experiments confirmed that all three classes of KIRAs are selective across the human kinome.

Our SAR studies suggest that the key to discriminating between the very similar ATP-binding sites of IRE1 α and IRE1 β is optimizing the KIRA substituent that is in close proximity to their gatekeeper residues, which is Ile in IRE1 α and Leu in IRE1 β . Altogether, KIRAs with differing selectivity profiles (highly IRE1 α -selective, dual-IRE1, and highly IRE1 β -selective) will serve as useful tools for work characterizing the specific outputs of IRE1 in cells and, potentially, in animal models of gastrointestinal and pulmonary ER stress-related diseases.

■ ASSOCIATED CONTENT

Supporting Information

The Supporting Information is available free of charge on the ACS Publications website at DOI: 10.1021/acscchembio.9b00482.

Supplemental Figures S1–S12, methods, protein amino acid sequence and DNA sequence, synthetic procedures, and inhibitor characterization (PDF)
Compound characterization checklist (XLSX)
Kinobead profiling data (XLSX)

■ AUTHOR INFORMATION

Corresponding Author

*E-mail: djmaly@uw.edu.

ORCID

Dustin J. Maly: 0000-0003-0094-0177

Notes

The authors declare the following competing financial interest(s): B.J.B., F.R.P., and D.J.M. are founders, equity holders, and consultants for OptiKIRA, LLC (Cleveland, OH), a biotech company focused on treating ER-stress-induced retinal degeneration.

■ ACKNOWLEDGMENTS

This work was supported by the National Institutes of Health (R01DK116064 and R01DK100623 (F.R.P. and D.J.M.)).

■ REFERENCES

- (1) Scheuner, D., and Kaufman, R. J. (2008) The Unfolded Protein Response: A Pathway That Links Insulin Demand with β -Cell Failure and Diabetes. *Endocr. Rev.* 29, 317–333.
- (2) van Anken, E., Pena, F., Hafkemeijer, N., Christis, C., Romijn, E. P., Grauschopf, U., Oorschot, V. M., Pertel, T., Engels, S., Ora, A., Lastun, V., Glockshuber, R., Klumperman, J., Heck, A. J., Luban, J., and Braakman, I. (2009) Efficient IgM assembly and secretion require the plasma cell induced endoplasmic reticulum protein pERp1. *Proc. Natl. Acad. Sci. U. S. A.* 106, 17019–17024.
- (3) Walter, P., and Ron, D. (2011) The unfolded protein response: from stress pathway to homeostatic regulation. *Science* 334, 1081–1086.
- (4) Tirasophon, W., Welihinda, A. A., and Kaufman, R. J. (1998) A stress response pathway from the endoplasmic reticulum to the nucleus requires a novel bifunctional protein kinase/endoribonuclease (Ire1p) in mammalian cells. *Genes Dev.* 12, 1812–1824.
- (5) Harding, H. P., Zhang, Y., and Ron, D. (1999) Protein translation and folding are coupled by an endoplasmic-reticulum-resident kinase. *Nature* 397, 271–274.
- (6) Haze, K., Yoshida, H., Yanagi, H., Yura, T., and Mori, K. (1999) Mammalian transcription factor ATF6 is synthesized as a transmembrane protein and activated by proteolysis in response to endoplasmic reticulum stress. *Mol. Biol. Cell* 10, 3787–3799.
- (7) Hetz, C., Chevet, E., and Oakes, S. A. (2015) Proteostasis control by the unfolded protein response. *Nat. Cell Biol.* 17, 829–838.

- (8) Travers, K. J., Patil, C. K., Wodicka, L., Lockhart, D. J., Weissman, J. S., and Walter, P. (2000) Functional and genomic analyses reveal an essential coordination between the unfolded protein response and ER-associated degradation. *Cell* 101, 249–258.
- (9) Shore, G. C., Papa, F. R., and Oakes, S. A. (2011) Signaling cell death from the endoplasmic reticulum stress response. *Curr. Opin. Cell Biol.* 23, 143–149.
- (10) Han, D., Lerner, A. G., Vande Walle, L., Upton, J. P., Xu, W., Hagen, A., Backes, B. J., Oakes, S. A., and Papa, F. R. (2009) IRE1alpha kinase activation modes control alternate endoribonuclease outputs to determine divergent cell fates. *Cell* 138, 562–575.
- (11) Wang, X. Z., Harding, H. P., Zhang, Y., Jolicoeur, E. M., Kuroda, M., and Ron, D. (1998) Cloning of mammalian Ire1 reveals diversity in the ER stress responses. *EMBO J.* 17, 5708–5717.
- (12) Ali, M. M., Bagratuni, T., Davenport, E. L., Nowak, P. R., Silva-Santisteban, M. C., Hardcastle, A., McAndrews, C., Rowlands, M. G., Morgan, G. J., Aherne, W., Collins, I., Davies, F. E., and Pearl, L. H. (2011) Structure of the Ire1 autophosphorylation complex and implications for the unfolded protein response. *EMBO J.* 30, 894–905.
- (13) Lee, K. P., Dey, M., Neculai, D., Cao, C., Dever, T. E., and Sicheri, F. (2008) Structure of the dual enzyme Ire1 reveals the basis for catalysis and regulation in nonconventional RNA splicing. *Cell* 132, 89–100.
- (14) Lu, Y., Liang, F. X., and Wang, X. (2014) A synthetic biology approach identifies the mammalian UPR RNA ligase RtcB. *Mol. Cell* 55, 758–770.
- (15) Kosmaczewski, S. G., Edwards, T. J., Han, S. M., Eckwahl, M. J., Meyer, B. I., Peach, S., Hesselberth, J. R., Wolin, S. L., and Hammarlund, M. (2014) The RtcB RNA ligase is an essential component of the metazoan unfolded protein response. *EMBO Rep.* 15, 1278–1285.
- (16) Calfon, M., Zeng, H., Urano, F., Till, J. H., Hubbard, S. R., Harding, H. P., Clark, S. G., and Ron, D. (2002) IRE1 couples endoplasmic reticulum load to secretory capacity by processing the XBP-1 mRNA. *Nature* 415, 92–96.
- (17) Hollien, J., Lin, J. H., Li, H., Stevens, N., Walter, P., and Weissman, J. S. (2009) Regulated Ire1-dependent decay of messenger RNAs in mammalian cells. *J. Cell Biol.* 186, 323–331.
- (18) Hollien, J., and Weissman, J. S. (2006) Decay of endoplasmic reticulum-localized mRNAs during the unfolded protein response. *Science* 313, 104–107.
- (19) Lerner, A. G., Upton, J. P., Praveen, P. V., Ghosh, R., Nakagawa, Y., Igarria, A., Shen, S., Nguyen, V., Backes, B. J., Heiman, M., Heintz, N., Greengard, P., Hui, S., Tang, Q., Trusina, A., Oakes, S. A., and Papa, F. R. (2012) IRE1alpha induces thioredoxin-interacting protein to activate the NLRP3 inflammasome and promote programmed cell death under irremediable ER stress. *Cell Metab.* 16, 250–264.
- (20) Upton, J. P., Wang, L., Han, D., Wang, E. S., Huskey, N. E., Lim, L., Truitt, M., McManus, M. T., Ruggero, D., Goga, A., Papa, F. R., and Oakes, S. A. (2012) IRE1alpha cleaves select microRNAs during ER stress to derepress translation of proapoptotic Caspase-2. *Science* 338, 818–822.
- (21) Bertolotti, A., Wang, X., Novoa, I., Jungreis, R., Schlessinger, K., Cho, J. H., West, A. B., and Ron, D. (2001) Increased sensitivity to dextran sodium sulfate colitis in IRE1beta-deficient mice. *J. Clin. Invest.* 107, 585–593.
- (22) Imagawa, Y., Hosoda, A., Sasaka, S.-I., Tsuru, A., and Kohno, K. (2008) RNase domains determine the functional difference between IRE1alpha and IRE1beta. *FEBS Lett.* 582, 656–660.
- (23) Nakamura, D., Tsuru, A., Ikegami, K., Imagawa, Y., Fujimoto, N., and Kohno, K. (2011) Mammalian ER stress sensor IRE1beta specifically down-regulates the synthesis of secretory pathway proteins. *FEBS Lett.* 585, 133–138.
- (24) Iwawaki, T., Hosoda, A., Okuda, T., Kamigori, Y., Nomura-Furuwatari, C., Kimata, Y., Tsuru, A., and Kohno, K. (2001) Translational control by the ER transmembrane kinase/ribonuclease IRE1 under ER stress. *Nat. Cell Biol.* 3, 158–164.
- (25) Martino, M. B., Jones, L., Brighton, B., Ehre, C., Abdulah, L., Davis, C. W., Ron, D., O'Neal, W. K., and Ribeiro, C. M. P. (2013) The ER stress transducer IRE1beta is required for airway epithelial mucin production. *Mucosal Immunol.* 6, 639–654.
- (26) Hauber, H.-P., Foley, S. C., and Hamid, Q. (2006) Mucin Overproduction in Chronic Inflammatory Lung Disease. *Can. Respir. J.* 13, 327–335.
- (27) Iqbal, J., Dai, K., Seimon, T., Jungreis, R., Oyadomari, M., Kuriakose, G., Ron, D., Tabas, I., and Hussain, M. M. (2008) IRE1beta Inhibits Chylomicron Production by Selectively Degrading MTP mRNA. *Cell Metab.* 7, 445–455.
- (28) Wang, L., Perera, B. G., Hari, S. B., Bhattacharai, B., Backes, B. J., Seeliger, M. A., Schurer, S. C., Oakes, S. A., Papa, F. R., and Maly, D. J. (2012) Divergent allosteric control of the IRE1alpha endoribonuclease using kinase inhibitors. *Nat. Chem. Biol.* 8, 982–989.
- (29) Feldman, H. C., Tong, M., Wang, L., Meza-Acevedo, R., Gobillot, T. A., Lebedev, I., Gliedt, M. J., Hari, S. B., Mitra, A. K., Backes, B. J., Papa, F. R., Seeliger, M. A., and Maly, D. J. (2016) Structural and Functional Analysis of the Allosteric Inhibition of IRE1alpha with ATP-Competitive Ligands. *ACS Chem. Biol.* 11, 2195–2205.
- (30) Papa, F. R., Zhang, C., Shokat, K., and Walter, P. (2003) Bypassing a kinase activity with an ATP-competitive drug. *Science* 302, 1533–1537.
- (31) Harrington, P. E., Biswas, K., Malwitz, D., Tasker, A. S., Mohr, C., Andrews, K. L., Dellamaggiore, K., Kendall, R., Beckmann, H., Jaekel, P., Materna-Reichelt, S., Allen, J. R., and Lipford, J. R. (2015) Unfolded Protein Response in Cancer: IRE1alpha Inhibition by Selective Kinase Ligands Does Not Impair Tumor Cell Viability. *ACS Med. Chem. Lett.* 6, 68–72.
- (32) Golkowski, M., Vidadala, R. S. R., Lombard, C. K., Suh, H. W., Maly, D. J., and Ong, S.-E. (2017) Kinobead and Single-Shot LC-MS Profiling Identifies Selective PKD Inhibitors. *J. Proteome Res.* 16, 1216–1227.
- (33) Bantscheff, M., Eberhard, D., Abraham, Y., Bastuck, S., Boesche, M., Hobson, S., Mathieson, T., Perrin, J., Raida, M., Rau, C., Reader, V., Sweetman, G., Bauer, A., Bouwmeester, T., Hopf, C., Kruse, U., Neubauer, G., Ramsden, N., Rick, J., Kuster, B., and Drewes, G. (2007) Quantitative chemical proteomics reveals mechanisms of action of clinical ABL kinase inhibitors. *Nat. Biotechnol.* 25, 1035–1044.
- (34) Golkowski, M., Perera, G. K., Vidadala, V. N., Ojo, K. K., Van Voorhis, W. C., Maly, D. J., and Ong, S. E. (2018) Kinome chemoproteomics characterization of pyrrolo[3,4-c]pyrazoles as potent and selective inhibitors of glycogen synthase kinase 3. *Mol. Omics* 14, 26–36.
- (35) Morita, S., Villalta, S. A., Feldman, H. C., Register, A. C., Rosenthal, W., Hoffmann-Petersen, I. T., Mehdi-zadeh, M., Ghosh, R., Wang, L., Colon-Negron, K., Meza-Acevedo, R., Backes, B. J., Maly, D. J., Bluestone, J. A., and Papa, F. R. (2017) Targeting ABL-IRE1alpha Signaling Spares ER-Stressed Pancreatic beta Cells to Reverse Auto-immune Diabetes. *Cell Metab.* 25, 1207.
- (36) Alexander, L. T., Möbitz, H., Drueckes, P., Savitsky, P., Fedorov, O., Elkins, J. M., Deane, C. M., Cowan-Jacob, S. W., and Knapp, S. (2015) Type II Inhibitors Targeting CDK2. *ACS Chem. Biol.* 10, 2116–2125.
- (37) Wiseman, R. L., Zhang, Y., Lee, K. P., Harding, H. P., Haynes, C. M., Price, J., Sicheri, F., and Ron, D. (2010) Flavonol Activation Defines an Unanticipated Ligand-Binding Site in the Kinase-RNase Domain of IRE1. *Mol. Cell* 38, 291–304.
- (38) Sanches, M., Duffy, N. M., Talukdar, M., Thevakumaran, N., Chiovitti, D., Canny, M. D., Lee, K., Kurinov, I., Uehling, D., Al-awar, R., Poda, G., Prakesch, M., Wilson, B., Tam, V., Schweitzer, C., Toro, A., Lucas, J. L., Vuga, D., Lehmann, L., Durocher, D., Zeng, Q., Patterson, J. B., and Sicheri, F. (2014) Structure and mechanism of action of the hydroxy-aryl-aldehyde class of IRE1 endoribonuclease inhibitors. *Nat. Commun.* 5, 4202.
- (39) Korennykh, A. V., Egea, P. F., Korostelev, A. A., Finer-Moore, J., Zhang, C., Shokat, K. M., Stroud, R. M., and Walter, P. (2009) The

unfolded protein response signals through high-order assembly of Ire1. *Nature* 457, 687–693.

(40) Joshi, A., Newbatt, Y., McAndrew, P. C., Stubbs, M., Burke, R., Richards, M. W., Bhatia, C., Caldwell, J. J., McHardy, T., Collins, I., and Bayliss, R. (2015) Molecular mechanisms of human IRE1 activation through dimerization and ligand binding. *Oncotarget* 6, 13019–13035.

(41) Colombano, G., Caldwell, J. J., Matthews, T. P., Bhatia, C., Joshi, A., McHardy, T., Mok, N. Y., Newbatt, Y., Pickard, L., Strover, J., Hedayat, S., Walton, M. I., Myers, S. M., Jones, A. M., Saville, H., McAndrew, C., Burke, R., Eccles, S. A., Davies, F. E., Bayliss, R., and Collins, I. (2019) Binding to an Unusual Inactive Kinase Conformation by Highly Selective Inhibitors of Inositol-Requiring Enzyme 1 α Kinase-Endoribonuclease. *J. Med. Chem.* 62, 2447–2465.

(42) Concha, N. O., Smallwood, A., Bonnette, W., Totoritis, R., Zhang, G., Federowicz, K., Yang, J., Qi, H., Chen, S., Campobasso, N., Choudhry, A. E., Shuster, L. E., Evans, K. A., Ralph, J., Sweitzer, S., Heering, D. A., Buser, C. A., Su, D.-S., and Deyoung, M. P. (2015) Long-Range Inhibitor-Induced Conformational Regulation of Human IRE1 Endoribonuclease Activity. *Mol. Pharmacol.* 88, 1011–1023.

(43) Fabrini, R., De Luca, A., Stella, L., Mei, G., Orioni, B., Ciccone, S., Federici, G., Lo Bello, M., and Ricci, G. (2009) Monomer–Dimer Equilibrium in Glutathione Transferases: A Critical Re-Examination. *Biochemistry* 48, 10473–10482.

(44) Grey, M. J., Cloots, E., Simpson, M. S., LeDuc, N., Serebrenik, Y. V., De Luca, H., De Sutter, D., Luong, P., Thiagarajah, J. R., Paton, A. W., Paton, J. C., Seeliger, M. A., Eyckerman, S., Janssens, S., and Lencer, W. I. (2019) IRE1 β negatively regulates IRE1 α signaling in response to endoplasmic reticulum stress, *BioRxiv*, 586305, <https://www.biorxiv.org/content/10.1101/586305v1>.